Hindawi

Research Article

Influence of Different Excavation Sequence of Double-Side Heading Method on Supporting Structure

Chengkun Ling,[1] Yanmei Ruan,[2] Pengbo Wu,[1] Jin Li,[1] Jin Zhao [ID],[3] and Bingxiang Yuan [ID][3]

[1]*China Railway Tenth Bureau Group Urban Rail Transit Engineering Co.,Ltd., Guangzhou 510000, Guangdong, China*
[2]*Guangzhou Metro Design and Research Institute Co., Ltd., Guangzhou 510030, Guangdong, China*
[3]*Guangdong University of Technology School of Civil and Transportation Engineering, Guangzhou 510006, Guangdong, China*

Correspondence should be addressed to Bingxiang Yuan; yuanbx@gdut.edu.cn

The double-side heading method is often used in the construction of large-span and large-section tunnels. The excavation of the pilot tunnel is complex, so the construction efficiency is low. Based on the underground excavation tunnel project of a subway in Guangzhou, the section excavation sequence of the traditional double-side heading method is optimized according to the actual situation. Midas/GTS software is used for finite element analysis, the displacement and internal force of ground settlement and support structure under two different section excavation sequences are calculated, and the calculation results are compared with the field monitoring data. The calculation results show that the influence of the two excavation sequences on the displacement of the supporting structure is not much different, but the influence on the internal force of the supporting structure is obviously different. The stress value of the supporting structure caused by the optimized excavation sequence is larger, especially the temporary inverted arch, but it is within the controllable range. The optimized excavation sequence increases the construction work surface, greatly improves the construction efficiency, and reduces the project cost, which can provide a reference for the construction of urban subway tunnels under similar engineering conditions in the future.

1. Introduction

With the rapid development of urban transportation facilities, more and more tunnel projects have emerged. Due to the relatively dense population and buildings on the ground in the city, many underground pipe piles foundations, and subway lines, tunnel engineering has high requirements for construction safety, and any carelessness may result in an accident [1, 2]. The construction of an underground tunnel will disturb the surrounding buildings (structures), which will lead to the deformation of buildings, and even threaten the life safety of relevant personnel in serious cases [3–5]. Therefore, the deformation and stability control of the underground tunnel is the key technical links in urban tunnel engineering [6–9].

Compared with other tunnel excavation methods, the double-side heading method has advantages in controlling

surface subsidence and surface horizontal displacement [10–12]. For the double-side heading method, many scholars at home and abroad had in-depth studies on the safety and stability of the structure [13–17], soil particle properties [18–22], and the deformation law of the surrounding rock [23–25] in the construction process using the methods of field monitoring [26–28], model experiment [29–31], and numerical simulation analysis [32–34], but there are few studies on the optimization of the construction method. Due to the number of excavation sections, complex construction process, high construction cost, and slow construction speed of the double-side heading method, it needs to be optimized [35]. Zeng [36] optimized the excavation section of the double-side heading method, increased the area of the upper excavation section, and improved the construction efficiency; Yang et al. [37] optimized the supporting structure of the tunnel crossing the pebble soil layer, which well

controlled the surface settlement and reduced the construction risk; Li et al. [38] optimized the construction step of double-side heading method, adopted the excavation form of upper and lower sections, reserved core rock pillars in the middle soil layer, accelerated the construction progress, and improved the overall stability of the tunnel.

The influence of the construction step on supporting structure has not been discussed in-depth in the above studies. Based on this, an underground excavation tunnel of a subway station in Guangzhou is taken as the engineering background of this article. The tunnel has a large cross-section, and there is a large height difference between the lower pilot tunnel of the transverse passage and the upper pilot tunnel of the main line tunnel when the construction is completed. It is difficult to transport workers, machines, and materials. Therefore, the excavation sequence has been optimized. Midas/GTS software was used for finite element analysis. Combined with the field monitoring data, the displacement and internal force of the supporting structure under different excavation sequences were compared to analyze the safety and stability of the structure. Finally, a reasonable excavation sequence was selected after careful consideration of construction cost, construction period, and construction safety. The optimized construction scheme not only ensured the safety and stability of tunnel structure but also greatly improved the construction efficiency, which provides some reference for tunnels under similar engineering conditions.

2. Engineering Overview

The underground excavation tunnel interval is located at about 300 m east of the intersection of West side of Whampoa Avenue and Xiancun Road, which is connected to the east end of Xiancun Station. Two open-cut shafts were set up, and the rest were underground excavation channel. The left line is 163.845 m long and goes through the Whampoa Avenue Tunnel in parallel, and the vault is about 16.9 m from the bottom of the Whampoa Avenue Tunnel. The right line is 51.72 m long and is laid below the south side of Whampoa Avenue, and the vault is about 25 m from the ground. The crossover between the left and right lines is 37.35 m long. The general layout of the underground excavation tunnel interval is shown in Figure 1.

The construction method for the tunnel adopted the double-side heading method. The construction sequence was to excavate the upper section, construct the supporting structure, and then excavate the lower section after the construction of the upper section was completed. The daily footage of construction was 1 m. The finite element model was modeled and analyzed based on this working condition.

3. Construction Optimization Scheme

The main principle of the double-side heading method is to divide the large section of the tunnel into small sections using the middle wall, and each small section can be divided into upper and lower pilot tunnels to avoid stress concentration. The specific section is shown in Figure 2. The common excavation sequence of sections is that the left and right sections are constructed first and the support system is formed in time, and then the middle section is constructed, namely, ①-④-②-⑤-③-⑥. The optimized excavation sequence of the section is to excavate the upper left and right pilot tunnels first, then the upper middle pilot tunnel, then the lower left and right pilot tunnels, and finally the lower middle pilot tunnel, namely, ①-②-③-④-⑤-⑥.

4. Numerical Simulation

4.1. Calculation Model and Boundary Conditions. The model strata from top to bottom were plain fill, medium coarse sand, plastic residual soil, strongly weathered pelitic siltstone, moderately weathered pelitic siltstone, and slightly weathered pelitic siltstone. The model included shaft, transverse passage, main line tunnel, and foundation pit above the tunnel. According to Saint-Venant's principle, when the size of the model is 3 to 5 times the tunnel span, the influence of the boundary effect on the model can be ignored [39]. Therefore, the boundary of the overall model was 120 m in the X direction, 140 m in the Y direction, and 50 m in the Z direction. The total number of model elements was 130161, and the total number of mesh nodes was 76573, as shown in Figure 3.

4.2. Material Constitutive and Parameters. The Mohr–Coulomb constitutive model was adopted for plain fill, medium coarse sand, plastic residual soil, and strongly weathered pelitic siltstone [40]. The moderately weathered and slightly weathered pelitic siltstone adopted the modified Mohr–Coulomb constitutive model because of their relatively complete rock structure and hard rock quality. Supporting structures such as shotcrete, bolt, grid steel frame, and section steel adopted the elastic constitutive model. The physical and mechanical parameters of each material are shown in Table 1.

The initial support of transverse passage and tunnel adopted the form of grid steel frame and shotcrete, and the elastic modulus of initial support was calculated by the method of stiffness equivalence [41]. The equivalent elastic modulus of initial support was calculated to be 25.382 Gpa, and the equivalent elastic modulus of the temporary support was 29.064 Gpa.

4.3. Simulated Construction Steps. The original construction scheme and the optimized construction scheme were compared using numerical simulation. The original construction scheme was scheme I and the optimized construction scheme was scheme II. The specific construction steps of scheme I were as follows (S stands for construction steps).

(1) Initial stress field analysis (IS): activate the original strata, gravity, and boundary condition in the numerical model and cleared the displacement to simulate the state when the tunnel was not excavated.

FIGURE 1: General layout of underground excavation tunnel interval.
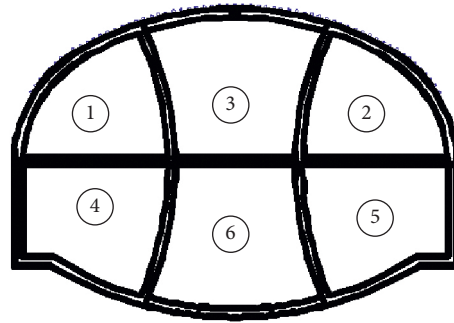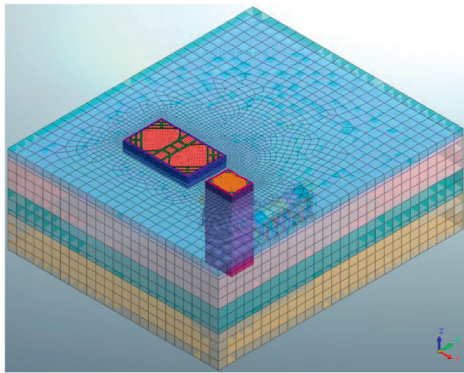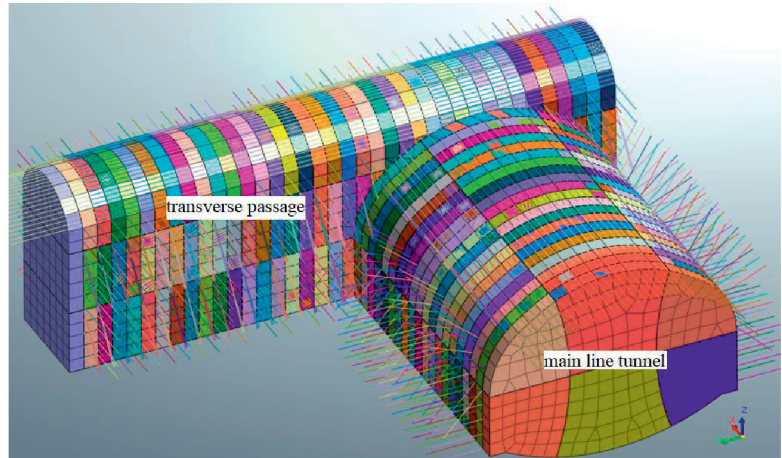

FIGURE 2: Construction process of double-side heading method.

(a)   (b)

FIGURE 3: Double-side heading method model. (a) Overall model. (b) Main tunnel model.

(2) Excavate shaft and foundation pit and construct the supporting structure (S2)

(3) Excavate the upper (S3–S40), middle (S41–S78), and lower (S79–S116) pilot tunnels of transverse passage and construct the supporting structure

(4) Excavate the 1 and 2 (S117), 4 and 5 (S118), 3 (S119), and 6 pilot tunnels (S120) of the mainline tunnel in sequence, and the supporting structures of each pilot tunnel were constructed after one construction step

Repeat the above steps until the construction was completed; scheme I included 159 construction steps in total.

The specific construction steps of scheme II were as follows:

(1) Initial stress field analysis (IS): activate the original strata, gravity, and boundary condition in the numerical model and clear the displacement to simulate the state when the tunnel was not excavated.

(2) Excavate the shaft and foundation pit and construct the supporting structure (S2).

(3) Excavate the upper (S3–S40) and middle (S41–S78) pilot tunnels of transverse passage and construct the supporting structure.

TABLE 1: Physicomechanical parameters of material.

Material name	Elastic modulus/ (MPa)	Bulk density/(kN/ m³)	Cohesion/ (kN/m²)	Internal friction angle/ (°)	Strata thickness /(m)
Plain fill	12.6	19.0	10.0	9.0	3.2
Medium-coarse sand	16.0	20.0	0	30.0	2.0
Plastic residual soil	22.0	22.0	18.6	18.0	14.6
Strongly weathered pelitic siltstone	50.0	21.0	45.0	30.0	10.0
Moderately weathered pelitic siltstone	200.0	25.6	180.0	32.0	2.2
Slightly weathered pelitic siltstone	400.0	26.0	450.0	35.0	18.0
C25 shotcrete	23000.0	25.0			
Initial support	25383.0	25.0			
Temporary support	29064.0	25.0			
Bolt	206000.0	78.5			

(4) Excavate the 1 and 2 (S79) and 3 pilot tunnels (S80) of the main line tunnel in sequence, and the supporting structures of each pilot tunnel were constructed after one construction step.

(5) Repeat the above steps until the construction of the upper section of main line tunnel is completed (S79–S99).

(6) Excavate the lower (S100–S137) pilot tunnel of transverse passage and construct the supporting structure.

(7) Excavat the 4 and 5 tunnels (S138) and 3 pilot tunnels (S80) of main line tunnel in sequence, and the supporting structure of each pilot tunnel were constructed after one construction step;

Repeat the above steps until the construction was completed, and scheme II included 159 construction steps in total.

5. Results

5.1. Analysis of Surface Settlement of Transverse Passage. After simulation calculation, the surface settlement curve of the transverse passage with the construction steps as the abscissa was drawn, as shown in Figure 4, where the monitoring section is $Y = 70$ m.

Figure 4 shows that the final surface settlement of the transverse passage is 11.77 mm. The biggest impact on the surface settlement of the transverse passage was the excavation of the upper pilot tunnel of the transverse passage, and the settlement value was about 8.22 mm, accounting for 69.8% of the total settlement value. The second was the excavation of the upper pilot tunnel of the main line tunnel, and the settlement value increased from 9.19 mm to 10.99 mm, accounting for 15.3% of the total settlement value. The excavation of the middle and lower pilot tunnels of the transverse passage and the lower pilot tunnel of the main line tunnel had little impact on the surface settlement of the transverse passage. The reason was that the initial support was timely constructed after the excavation of the upper section, which played a role in supporting and limiting the vertical displacement of the soil. Therefore, the excavation of the upper pilot tunnel of the transverse passage

was a key construction process, and monitoring should be strengthened during on-site construction.

The surface settlement data of the transverse passage at section $Y = 70$ m in the numerical model was selected for comparison and analysis with the field monitoring data. The on-site construction progress was that the construction of the upper pilot tunnel of the transverse passage had been completed, and the middle pilot tunnel had been excavated for 6 m. The comparison results are shown in Figure 5.

Figure 5 shows that the trend of the surface settlement results of the transverse passage in the field monitoring data and numerical simulation was basically the same, but the settlement value of field monitoring was larger than the numerical simulation. The final settlement value of field monitoring was 13.69 mm, which was 66.6% larger than the result of the numerical simulation. The reason why the numerical simulation results were small was that the model ignored the influence of groundwater [42, 43]. Only self-weight stress was considered in rock and soil mass, and the influence of tectonic stress was ignored. The deformation of rock and soil mass was considered to be isotropic. These simplifications and assumptions made the numerical simulation results smaller than the actual settlement value.

5.2. Displacement Analysis of Initial Support of Tunnel. The displacement value of initial support was extracted according to the monitoring points shown in Figure 6, where the monitoring surface was located at $X = 50$ m and the corresponding tunnel excavation distance was 10 m. Figure 7 shows the displacement diagram of initial support under different schemes. As can be seen from the figure, the settlement value from large to small of the tunnel was vault, spandrel, hance, and arch foot. The settlement value of the right initial support was slightly larger than that of the left because there was a foundation pit above the left initial support, which reduced the soil press upside, so the settlement of the left initial support was smaller. For scheme I, when the excavation surface did not reach the monitoring surface, some areas of the monitoring point had slight displacement. After the excavation reached the monitoring surface, the displacement of the initial support increased with the advancement of the excavation surface and finally tended to be stable.
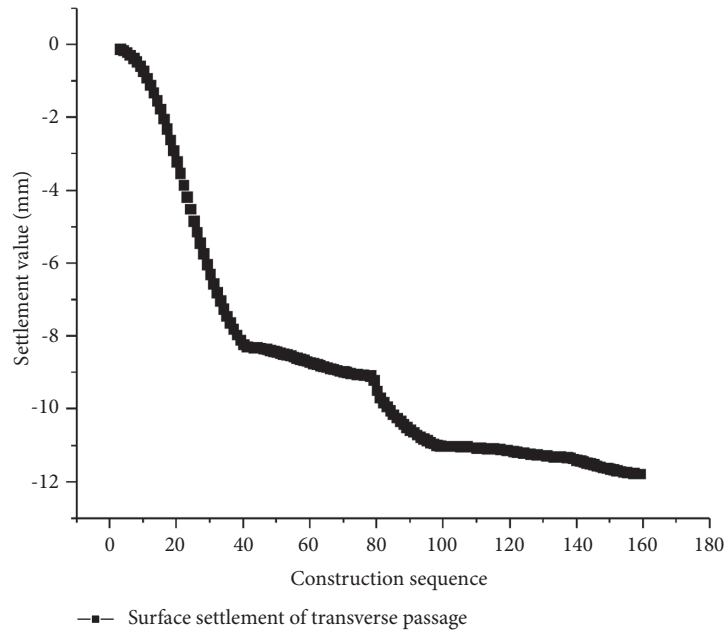
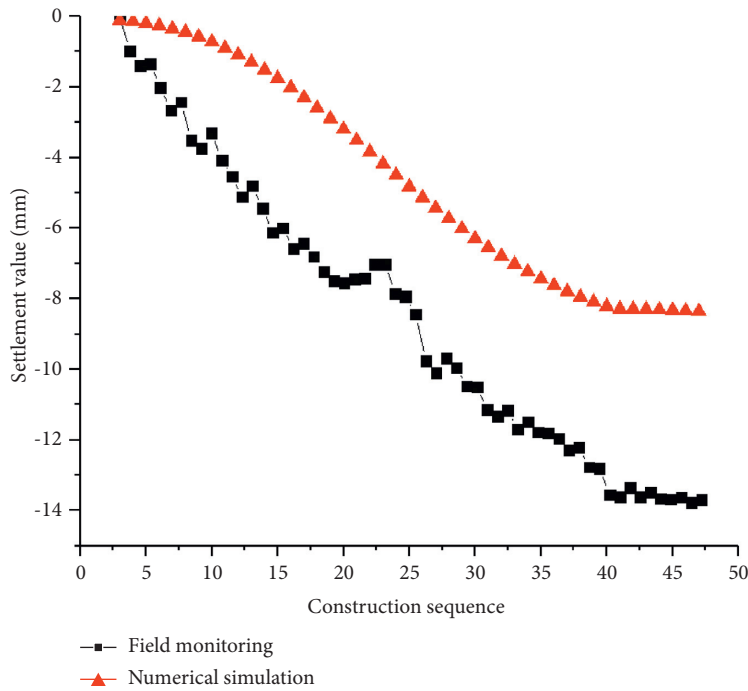FIGURE 4: Time-history curve of surface settlement of transverse passage.

FIGURE 5: Comparison of the time-history curve of surface settlement of transverse passage.

For scheme II, the influence of tunnel excavation on the initial support was divided into two parts. The first part was the excavation of the upper section of the tunnel. At this time, the vault and spandrel had a large settlement, and the settlement of the hance was small. The second part was the excavation of the lower section of the tunnel, which had a small impact on the overall initial support. The excavation of the lower pilot tunnel of the transverse passage had little effect on the displacement of the tunnel initial support. The

final displacement values of each monitoring point of tunnel initial support under different construction schemes are shown in Table 2.

Table 2 shows that the settlement values of the vault and left and right arch feet in scheme II were 4.6%, 77.8%, and 44.1%, lower than those in scheme I, while the settlement values of the left and right spandrels and hance were 16.4%, 17.7%, and 56.1%, 58.9% higher than those in scheme I, respectively, and the uplift value of the arch bottom was
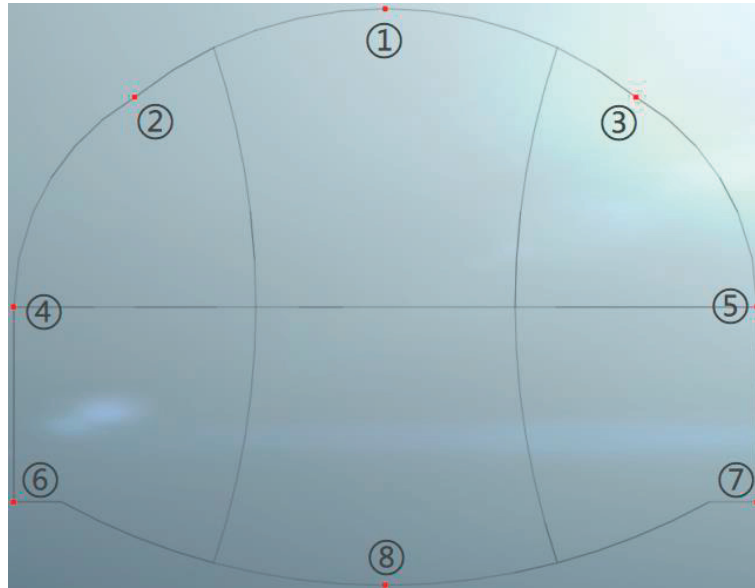
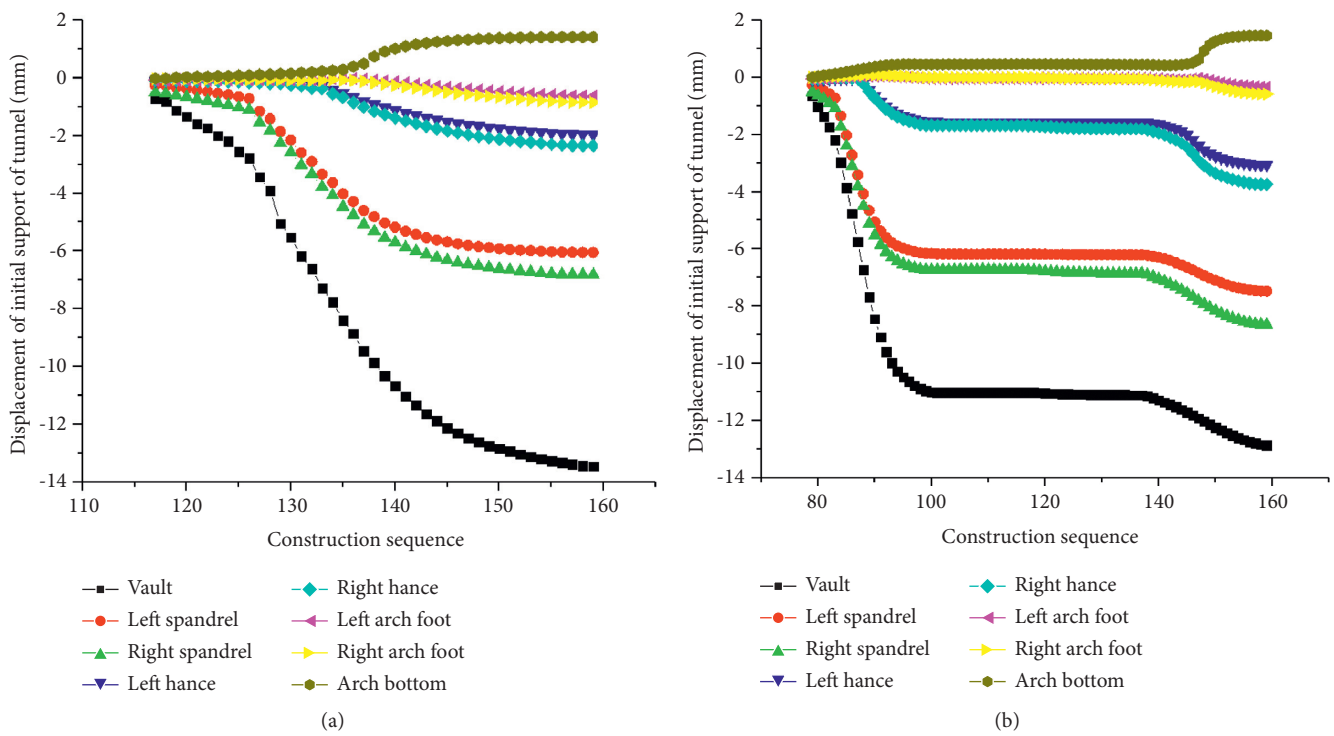FIGURE 6: Layout diagram of initial support monitoring points.

(a)

(b)

FIGURE 7: Time-history curves of tunnel initial support displacement under different schemes. (a) Time-history curve of tunnel initial support displacement in scheme I. (b) Time-history curve of tunnel initial support displacement in scheme II.

3.5% higher than that in scheme I. The displacement values of the hance and arch foot of the two construction schemes were quite different. The reason was that scheme I was to excavate the sections on both sides first and then excavate the middle section after the initial support on both sides forms a closed loop; scheme II was to excavate the upper section first and then excavate the lower section after the upper section was completed. The support construction sequences of the two construction schemes were different, so the stress conditions of the hance and arch foot were quite different, and the final settlement value was also quite different.

To sum up, the displacement law of initial support caused by different excavation sequences was roughly the same. Scheme II had a slightly greater impact on the displacement of initial support, but within the controllable

TABLE 2: Final displacement value of monitoring points in initial support of tunnel unit: mm.

Scheme	①	②	③	④	⑤	⑥	⑦	⑧
I	−13.4	−6.1	−6.8	−2.0	−2.4	−0.6	−0.9	1.4
II	−12.8	−7.0	−8.0	−3.1	−3.8	−0.4	−0.6	1.5

range. The excavation of 3-pilot tunnel was a key construction process, so it needed to do well in advance support and timely constructed initial support to control the vertical displacement. The excavation of the lower pilot tunnel of the transverse passage had little effect on the completed tunnel support.

5.3. Stress Analysis of Tunnel Supporting Structure.
Figure 8 shows the cloud diagram of the major principle stress of supporting structure when the tunnel excavation of different schemes was completed. As seen from the figure, the major principal stress distribution and value of the tunnel supporting structure of the two schemes were basically the same. In terms of initial support, most of the spandrel and hance were compressed, and a small part was tensioned at the front of the tunnel. Most of the vault and arch bottom were compressed, and a small part was tensioned at the end of the tunnel. In terms of temporary support, most of the temporary inverted arch and the middle wall were tensioned; the part of the temporary inverted arch near both ends of the tunnel and the middle wall near the temporary inverted arch would be compressed. The stress value of the middle wall of the tunnel was greater than that of the temporary inverted arch, and the stress value of the upper middle wall was greater than that of the lower middle wall.

5.3.1. Initial Support of 1-Pilot Tunnel.
The stress value of initial support was extracted according to the monitoring points shown in Figure 9, where the monitoring surface was located at $X = 45$ m, and the corresponding tunnel excavation distance was 5 m. As seen in Figure 8, the stress value of the initial support was symmetrical, so only the left initial support was selected for analysis.
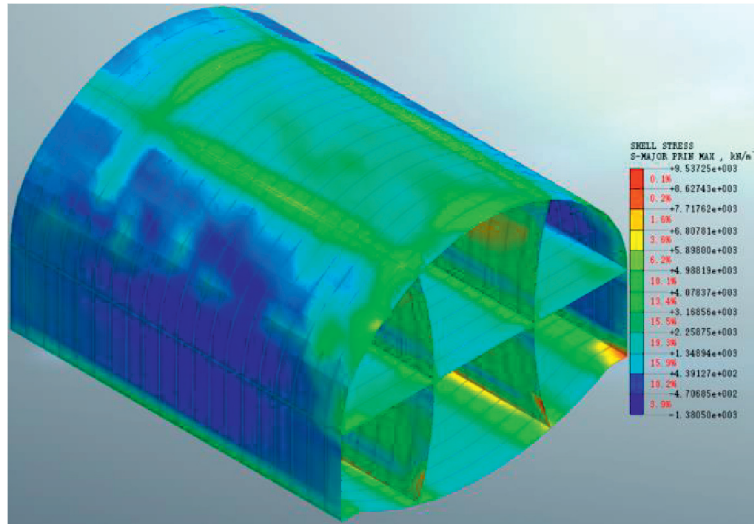
Figure 10(a) shows the time-history curve of initial support stress of the 1-pilot tunnel in scheme II. As seen from the figure, the stress value of the initial support of the 1-pilot tunnel decreased with the excavation of the upper section, and the stress value changed from positive to negative when the excavation reached the end of the upper section. Then, the lower pilot tunnel, different from the transverse passage, was excavated, and the excavation on the side close to the tunnel would slightly increase the compressive stress of the initial support. After the excavation surface passed through the tunnel surface, the stress value of the initial support remained stable. Finally, the lower section of the tunnel was excavated. When the excavation surface had not reached the monitoring surface, the compressive stress value of the initial support increased with the section excavation. After the excavation surface passed through the

monitoring surface, the stress value of the initial support basically remained stable.

The time-history curves of the initial support stress of the 1-pilot tunnel of two schemes were compared. Since the excavation of the lower pilot tunnel of the transverse passage had little effect on the stress value of the initial support, this part of the data was discarded during the comparison, and the construction steps were reordered. The comparison of the time-history curve of the initial support stress of the 1-pilot tunnel in the two schemes is shown in Figure 10(b). It could be seen that the variation law of stress value of the initial support of the two construction schemes was basically the same. The stress values of each monitoring point of tunnel initial support under different construction schemes are shown in Table 3. As can be seen from the table, the maximum tensile stress of scheme II was 7.7% higher than that of scheme I, and the maximum compressive stress was 240% higher than that of scheme I. Therefore, the first construction of the supporting structure on both sides could timely distribute the surrounding rock pressure to the lower support, reduced the stress value on the initial support, and was more conducive to the safety of the structure.

5.3.2. Temporary Inverted Arch of 1-Pilot Tunnel.
The stress value of the temporary inverted arch was extracted according to the monitoring points shown in Figure 9. As can be seen from Figure 11, the stress value of the temporary inverted arch of the 1-pilot tunnel in scheme I increased rapidly during early excavation and then decreased slowly with tunnel excavation. The stress value of the temporary inverted arch of the 1-pilot tunnel in scheme II increased continuously when excavating the upper section of the tunnel and reached the peak when excavating the end of the upper section. Then, the excavation of the lower section of the tunnel would rapidly reduce the stress value of the temporary inverted arch and continue to decrease with the excavation. As shown in Table 3, the maximum stress value and the stress value at the completion of tunnel excavation of the temporary inverted arch in scheme II were 173% and 101% higher than those in scheme I, respectively. The stress value of the temporary inverted arch in scheme I would be much less than that in scheme II because the supporting structure on both sides was excavated first. The stress value of the temporary inverted arch in scheme I would be much less than that in scheme II because the supporting structure on both sides was excavated first, and the stress system of the closed space could be formed more quickly.

5.3.3. Middle Wall of 1-Pilot Tunnel.
As can be seen from Figure 12, the overall trend of the stress value of the middle wall in 1-pilot tunnel of the two schemes increased first and then decreased slowly. The difference was that scheme II would cause disturbance to the middle wall when excavating the upper and lower sections, respectively, and the stress value had two fluctuation points.

(a)
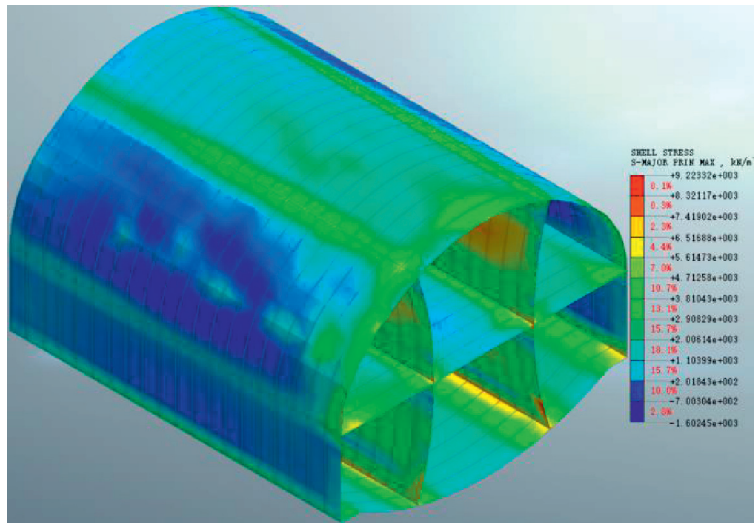
(b)

FIGURE 8: Different schemes of tunnel supporting structure major principle stress cloud diagram. (a) Tunnel supporting structure major principle stress cloud diagram of scheme I. (b) Tunnel supporting structure major principle stress cloud diagram of scheme II.
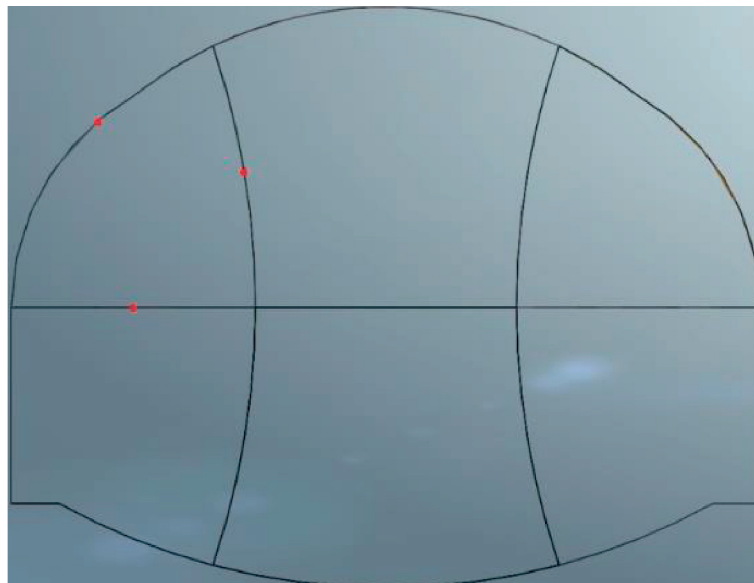

FIGURE 9: The stress value monitoring point layout of supporting structure.
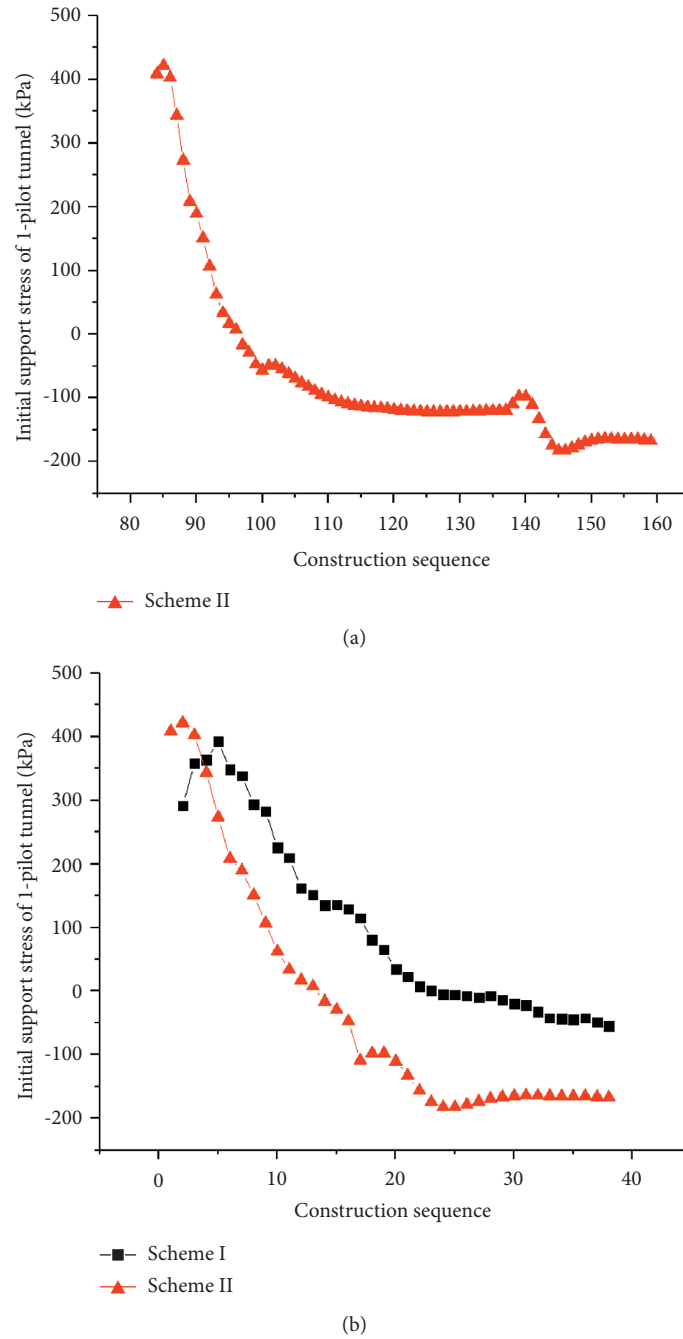
Figure 10: Time-history curve of initial support stress of 1-pilot tunnel. (a) Time-history curve of the initial support stress of 1-pilot tunnel in scheme II. (b) The comparison of time-history curve of the initial support stress of 1-pilot tunnel in the two schemes.

Table 3: Stress value of each monitoring point of tunnel supporting structure unit: MPa.

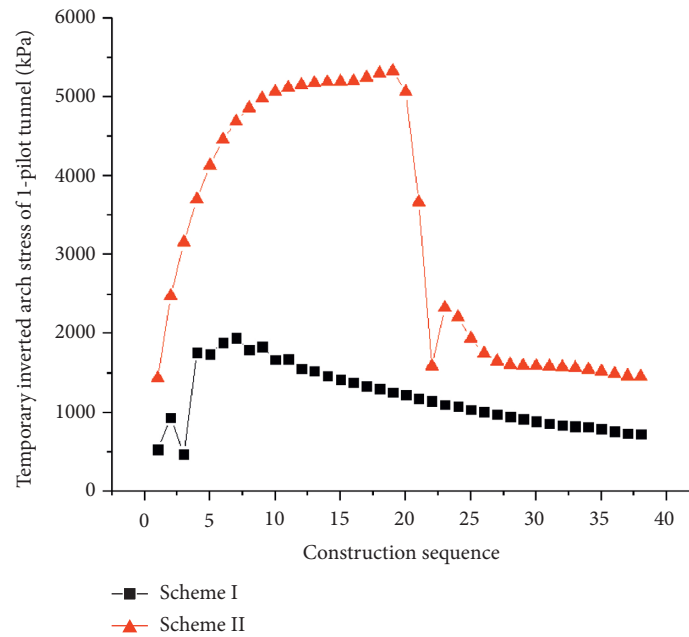| Scheme	Maximum stress value of initial support	Stress value at the completion of initial support excavation	Maximum stress value of temporary inverted arch	Stress value at the completion of temporary inverted arch excavation	Maximum stress value of middle wall	Stress value at the completion of middle wall excavation
I	0.39	−0.05	1.95	0.72	7.77	6.17
II	0.42	−0.17	5.33	1.45	8.73	6.51

FIGURE 11: Time-history curve of temporary inverted arch stress of 1-pilot tunnel.
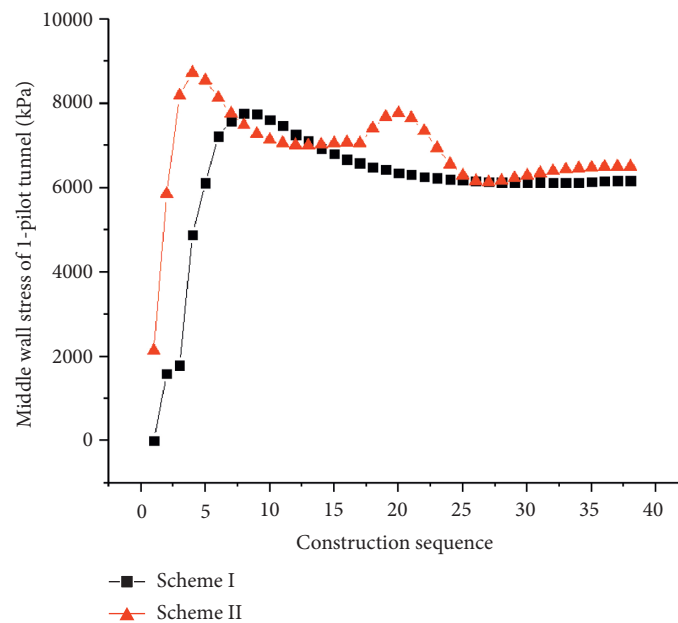

FIGURE 12: Time-history curve of middle wall stress of 1-pilot tunnel.

As shown in Table 3, the maximum stress value and the stress value at the completion of tunnel excavation of the middle wall in scheme II were 12.4% and 5.5% higher than those in scheme I, respectively.

To sum up, the stress values of initial support and temporary support in scheme II were higher than those in scheme I, but both were within the controllable range. Therefore, when scheme II was adopted for construction, it was necessary to strengthen the monitoring of the supporting structure, especially the temporary inverted arch, to ensure the construction safety.

5.3.4. Overall Comparison. Figure 13 shows the overall stress diagram of the tunnel support structure when the tunnel was excavated at 10 m according to different schemes. The stress of the tunnel support structure in scheme I was small in the spandrel, hance, and temporary inverted arch, and the stress was mainly concentrated in the vault, middle wall, arch foot, and arch bottom. The maximum tensile stress was 7.71 MPa located in the middle wall on the right side. The maximum compressive stress was −0.65 MPa located in the initial support on the right side. Because of the construction off the upper part of the supporting structure only,
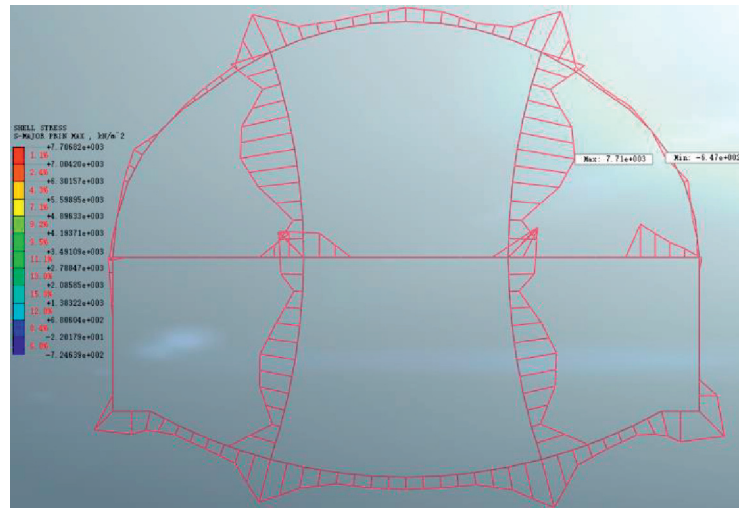
(a)
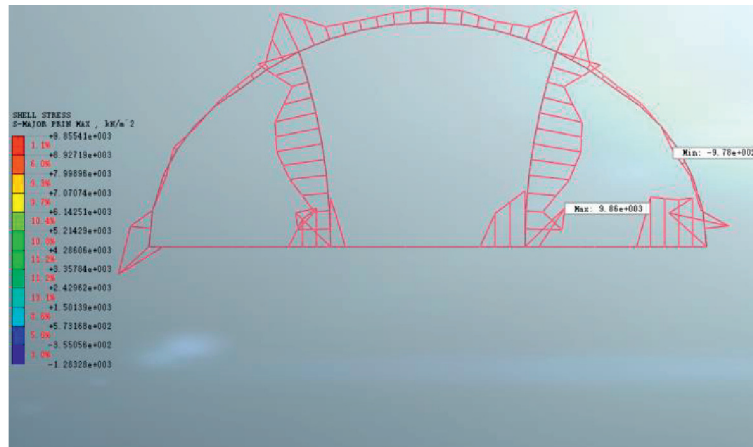
(b)

FIGURE 13: Overall stress diagram of the tunnel support structure. (a) Overall stress diagram of the tunnel support structure in scheme I. (b) Overall stress diagram of the tunnel support structure in scheme II.

the stress of hance and temporary inverted arch in scheme II were larger than that in scheme I. The maximum tensile stress was 9.86 MPa located in the temporary inverted arch on the right side. The maximum compressive stress was −0.98 MPa located in the initial support on the right side. Therefore, the lower part of the structure could share the load of the upper part of the structure and improve the safety and stability of the overall structure.

6. Conclusion

According to the numerical simulation data, after analyzing the surface displacement, displacement, and stress characteristics of the supporting structure of the double-side heading method under different excavation sequences, the conclusions were as follows:

(1) By comparing the numerical simulation date and monitoring data of transverse passage surface settlement, it could be seen that the variation law of surface settlement between the two methods was the same, which showed that the simulation of the deformation law of the stratum by this model was basically consistent. Based on this model, the excavation sequence of the double-side heading method could be qualitatively researched.

(2) Compared with the original construction scheme, the optimized construction scheme had a higher impact on the supporting structure, especially the temporary inverted arch, but it was within the controllable range. The optimized construction scheme first excavated the upper section of the tunnel and then the lower section, which solved the problems of the large height difference in the tunnel and difficulty in transporting workers, machines, and materials, increased the construction work surface, greatly improved the construction efficiency, and shortened the construction period. The optimized construction scheme can provide a reference for the construction of urban subway tunnels under similar engineering conditions in the future.

Data Availability

All data, models, or codes that support the findings of this study are available from the corresponding author upon reasonable request.

Conflicts of Interest

The authors declare that they have no conflicts of interest.

Acknowledgments

References

[1] B. B. Yang and Y. Liu, "Application of fractals to evaluate fractures of rock due to mining," *Fractal and Fractional*, vol. 6, no. 2, pp. 1–15, 2022.

[2] B. Yang, S. Du, X. Zhao, D. Tang, and C. Yang, "Decision making of curriculum attainment degree for engineering geology based on fuzzy set theory," *Advances in Civil Engineering*, vol. 2021, Article ID 1743778, 6 pages, 2021.

[3] B. Yuan, Z. Li, Z. Zhao, H. Ni, Z. Su, and Z. Li, "Experimental study of displacement field of layered soils surrounding laterally loaded pile based on Transparent Soil," *Journal of Soils and Sediments*, vol. 21, no. 9, pp. 3072–3083, 2021.

[4] X. Que, Z. Zhu, Z. Niu, and W. Lu, "Estimating the strength and deformation of columnar jointed rock mass based on physical model test," *Bulletin of Engineering Geology and the Environment*, vol. 80, no. 2, pp. 1557–1570, 2021.

[5] Y.-C. Guo, Y.-Y. Ye, G. Guan-Lin, J.-F. Lv, Y.-L. Bai, and J.-J. Zeng, "Effective usage of high strength steel tubes: Axial compressive behavior of hybrid FRP-concrete-steel solid columns," *Thin-Walled Structures*, vol. 154, Article ID 106796, 2020.

[6] B. Yuan, Z. Li, Z. Su, Q. Luo, M. Chen, and Z. Zhao, "Sensitivity of multistage fill slope based on finite element model," *Advances in Civil Engineering*, vol. 2021, Article ID 6622936, 13 pages, 2021.

[7] B. Yang, J. Liu, X. Zhao, and S. Zheng, "Evaporation and cracked soda soil improved by fly ash from recycled materials," *Land Degradation & Development*, vol. 32, no. 9, pp. 2823–2832, 2021.

[8] J. Xiao, X. Long, W. Qu, L. Li, H. Jiang, and Z. Zhong, "Influence of sulfuric acid corrosion on concrete stress-strain relationship under uniaxial compression," *Measurement*, vol. 187, Article ID 110318, 2022.

[9] J. Xiao, Z. M. Xu, Y. K. Murong et al., "Effect of chemical composition of fine aggregate on the frictional behavior of concrete–soil interface under sulfuric acid environment," *Fractal Fract*, vol. 6, no. 1, pp. 1–23, 2022.

[10] C. Liu, "Analysis of influence of different excavation methods on stability of highway tunnel," *Highway Engineer*, vol. 44, no. 1, pp. 130–134, 2019.

[11] Y. C. Zhang, G. W. Hu, and Z. X. Xin, "Comparative analysis and selection of construction methods for large section loess tunnel," *Journal of Railway Engineering Society*, vol. 27, no. 3, pp. 87–92, 2010.

[12] J. Y. Liu, G. Lv, M. Q. Zhang, L. Yue, and D. H. Luo, "Study on extra-large span tunnel excavation methods for Badaling Great Wall station of Beijing-Zhangjiakou high-speed railway," *Modern Tunnelling Technology*, vol. 56, no. S2, pp. 578–584, 2019.

[13] F. Liu, W. Zheng, L. Li, W. Feng, and G. Ning, "Mechanical and fatigue performance of rubber concrete," *Construction and Building Materials*, vol. 47, pp. 711–719, 2013.

[14] F. Liu, G. Chen, L. Li, and Y. Guo, "Study of impact performance of rubber reinforced concrete," *Construction and Building Materials*, vol. 36, no. 11, pp. 604–616, 2012.

[15] W. Feng, F. Liu, F. Yang, L. Li, and L. Jing, "Experimental study on dynamic split tensile properties of rubber concrete," *Construction and Building Materials*, vol. 165, pp. 675–687, 2018.

[16] Y. Guo, J. Xie, J. Zhao, and K. Zuo, "Utilization of unprocessed steel slag as fine aggregate in normal- and high-strength concrete," *Construction and Building Materials*, vol. 204, pp. 41–49, 2019.

[17] Y. C. Guo, S. H. Xiao, J. J. Zeng, J. Y. Su, T. Z. Li, and Z. H. Xie, "Behavior of concrete-filled FRP tube columns internally reinforced with FRP-steel composite bars under axial compression," *Construction and Building Materials*, vol. 315, pp. 1–18, Article ID 125714, 2022.

[18] Y. Wu, J. Cui, J. Huang, W. Zhang, N. Yoshimoto, and L. Wen, "Correlation of critical state strength properties with particle shape and surface fractal dimension of clinker ash," *International Journal of Geomechanics*, vol. 21, no. 6, Article ID 04021071, 2021.

[19] B. Bai, Q. Nie, Y. Zhang, X. Wang, and W. Hu, "Cotransport of heavy metals and SiO2 particles at different temperatures by seepage," *Journal of Hydrology*, vol. 597, Article ID 125771, 2021.

[20] L. Wang, G. Li, X. Li et al., "Influence of reactivity and dosage of MgO expansive agent on shrinkage and crack resistance of face slab concrete," *Cement and Concrete Composites*, vol. 126, Article ID 104333, 2022.

[21] L. Wang, X. F. Song, H. M. Yang et al., "Pore structural and fractal analysis of the effects of MgO reactivity and dosage on permeability and F–T resistance of concrete," *Fractal and Fractional*, vol. 6, no. 2, pp. 1–17, 2022.

[22] L. Wang, R. Y. Luo, W. Zhang, M. M. Jin, and S. W. Tang, "Effects of fineness and content of phosphorus slag on cement hydration, permeability, pore structure and fractal dimension of concrete," *Fractals*, vol. 29, no. 2, Article ID 2140004, 2021.

[23] B. X. Yuan, M. Sun, L. Xiong, Q. Z. Luo, S. P. Pradhan, and H. Z. Li, "Investigation of 3D deformation of transparent soil around a laterally loaded pile based on a hydraulic gradient model test," *Journal of Building Engineering*, vol. 28, no. 3, Article ID 1010124, 2020.

[24] B. Yuan, M. Sun, Y. Wang, L. Zhai, Q. Luo, and X. Zhang, "Full 3D displacement measuring system for 3D displacement field of soil around a laterally loaded pile in transparent soil," *International Journal of Geomechanics*, vol. 19, no. 5, Article ID 04019028, 2019.

[25] B. Yuan, L. Xiong, L. Zhai et al., "Transparent synthetic soil and its application in modeling of soil-structure interaction using optical system," *Frontiers of Earth Science*, vol. 7, p. 276, 2019.

[26] S. T. Li, Z. S. Tan, and W. T. Du, "Analysis on the mechanical behavior of the small spacing highway tunnel with super large cross section," *China Civil Engineering Journal*, vol. 50, no. S2, pp. 292–296, 2017.

[27] W. Zhou, "Scheme optimization and monitoring analysis of large section shallow buried tunnel on existing highway,"

Journal of Xi'an University of Architecture and Technology, vol. 52, no. 4, pp. 520–527, 2020.

[28] D. P. Ren, "Construction technology of variable Cross-section for Three-line bifurcation and Large-span section of railway tunnel," *Railway Engineering*, vol. 61, no. 12, pp. 105–108, 2021.

[29] S. Q. Liu, J. H. Guo, Y. Yue, and H. W. Shen, "Influence simulation of different underground excavation methods on surface settlement for underground station built in hard rock area," *Urban Mass Transit*, vol. 24, no. 3, pp. 142–146, 2021.

[30] N. Liu, K. Chen, X. Y. Liu, and S. H. Fu, "Study on excavation technology of rock column in double tunnel of subway station," *Journal of Railway Science and Engineering*, vol. 17, no. 9, pp. 2320–2327, 2020.

[31] L. C. Yang, S. H. Zhou, and Y. M. Yao, "Ground surface settlement during excavation of variety span tunnel," *Journal of Tongji University*, vol. 04, pp. 408–412, 2003.

[32] W. Deng, X. F. Shi, G. L. Yang, and H. Q. Zhang, "Analysis of numerical modeling and mechanical characteristics of large section tunnel," *Highway*, vol. 63, no. 3, pp. 253–259, 2018.

[33] Y. L. Zhang, G. Y. Wang, Z. Q. Li, and X. P. Wu, "The study on the influence of excavation parameters of deep buried and large-section tunnel," *Construction Technology*, vol. 43, no. S2, pp. 116–119, 2014.

[34] B. Zhu and X. J. Shi, "Study on construction of long span and soft rock tunnel with numerical simulation," *Applied Mechanics and Materials*, vol. 2733, pp. 438-439, 2013.

[35] Y. L. Shang and Z. Tan, "Optimization of mined construction method for the super-large section Liuhualu station of Guangzhou metro," *Modern Tunnelling Technology*, vol. 56, no. 3, pp. 177–185, 2019.

[36] S. Zeng, "Construction procedure optimization of double-sidewall guide pit method for large-section subsurface excavation subway station," *Municipal Engineer*, vol. 41, no. 1, pp. 152–155, 2019.

[37] Y. Yang, J. L. Huang, B. H. Wan, R. J. Liang, X. J. Wei, and X. Cai, "Research on construction optimization of shallow buried large section railway tunnel crossing pebble soil," *Journal of Railway Science and Engineering*, vol. 18, no. 5, pp. 1240–1247, 2021.

[38] X. D. Li and W. Wang, "Case study on construction of shallow metro tunnel by double side heading method with core rock kept," *Tunnel Construction*, vol. 35, no. 10, pp. 1060–1065, 2015.

[39] H. Rohola, "Advance numerical simulation of tunneling by using a double shield TBM," *Computers and Geotechnics*, vol. 57, 2014.

[40] B. X. Yuan, Z. H. Li, Y. M. Chen et al., "Mechanical and microstructural properties of recycling granite residual soil reinforced with glass fiber and liquid-modified polyvinyl alcohol polymer," *Chemosphere*, vol. 268, no. P1, Article ID 131652, 2021.

[41] Z. Song, Z. Cao, J. Wang, S. Wei, S. Hu, and Z. Niu, "Optimal analysis of tunnel construction methods through cross passage from subway shaft," *Advances in Civil Engineering*, vol. 2018, no. 3, Article ID 5181954, 14 pages, 2018.

[42] B. X. Yuan, Z. J. Li, W. J. Chen et al., "Influence of groundwater depth on pile–soil mechanical properties and fractal characteristics under cyclic loading," *Fractal Fractional*, vol. 6, no. 4, pp. 1–20, 2022.

[43] B. Bai, R. Zhou, G. Cai, W. Hu, and G. Yang, "Coupled thermo-hydro-mechanical mechanism in view of the soil particle rearrangement of granular thermodynamics," *Computers and Geotechnics*, vol. 137, no. 8, Article ID 104272, 2021.